LATE-STAGE FALL DEPOSITS OF THE BISHOP TUFF: MELT INCLUSION AND

CRYSTAL TEXTURAL INSIGHTS INTO THE LATE-STAGE STORAGE AND

EVACUATION OF A SUPERVOLCANIC MAGMA SYSTEM

by

ANNE A. FULTON

A THESIS

Presented to the Department of Earth Sciences
and the Graduate School of the University of Oregon
in partial fulfillment of the requirements
for the degree of
Master of Science

June 2019

THESIS APPROVAL PAGE

Student: Anne A. Fulton

Title: Late-Stage Fall Deposits of the Bishop Tuff: Melt Inclusion and Crystal Textural Insights into The Late-Stage Storage and Evacuation of a Supervolcanic Magma System

This thesis has been accepted and approved in partial fulfillment of the requirements for the Master of Science degree in the Department of Earth Sciences by:

Paul Wallace	Advisor
James Watkins	Chairperson
Ilya Bindeman	Member

and

Janet Woodruff-Borden	Vice Provost and Dean of the Graduate School

Original approval signatures are on file with the University of Oregon Graduate School.

Degree awarded June 2019

THESIS ABSTRACT

Anne A. Fulton

Master of Science

Department of Earth Sciences

June 2019

Title: Late-Stage Fall Deposits of the Bishop Tuff: Melt Inclusion and Crystal Textural Insights into The Late-Stage Storage and Evacuation of a Supervolcanic Magma System

To investigate the late-stage dynamics of the eruption of a compositionally and thermally zoned magma body, we targeted crystal-scale features in the stratigraphically latest fall unit (F9) of the 0.765 Ma Bishop Tuff. Spatial and temporal connections between the crystal-poorer, more-evolved ignimbrite to the east of Long Valley caldera and the crystal-richer, less-evolved ignimbrites to the north remain debated. From F9, we present major and trace elements and volatile data from quartz-hosted melt inclusions (MI) and matrix glasses, plus cathodoluminescence images and diffusion models of quartz phenocrysts. MI and textural data demonstrate that unit F9 is the fall equivalent of the northern and eastern ignimbrite lobes. This result confirms that these major ignimbrite packages, once considered sequential, were erupted coevally. The compositional record from MIs and crystal zoning in F9 implies the presence of multiple inputs of less evolved magmas to the system centuries to millennia before eruption. Major and trace element abundances for MIs and matrix glasses are included in a supplemental file.

CURRICULUM VITAE

NAME OF AUTHOR: Anne A. Fulton

GRADUATE AND UNDERGRADUATE SCHOOLS ATTENDED:

> University of Oregon, Eugene
> Pomona College, Claremont

DEGREES AWARDED:

> Master of Science, Earth Sciences, 2019, University of Oregon
> Bachelor of Arts, Geology, 2015, Pomona College

AREAS OF SPECIAL INTEREST:

> Geochemistry
> Volcanology

PROFESSIONAL EXPERIENCE:

> Graduate Teaching Fellow, University of Oregon, 2016-2019

> Post-Baccalaureate Research Assistant, Pomona College, 2015-2016

GRANTS, AWARDS, AND HONORS:

> Earth Sciences Emeritus Faculty Tribute Award, University of Oregon, 2018

> Earth Sciences Emeritus Faculty Tribute Award, University of Oregon, 2017

> Promising Scholar Award, University of Oregon, 2016

> Mason L. Hill Memorial Award in Geology, Pomona College, 2015

> Keck Geology Consortium Research Fellowship, 2014

> Zenger Award in Student Leadership, Pomona College, 2014

ACKNOWLEDGMENTS

TABLE OF CONTENTS

SUPPLEMENTAL FILES
    SPREADSHEET: MAJOR AND TRACE ELEMENT DATA

LIST OF FIGURES

LIST OF TABLES

CHAPTER I

INTRODUCTION/GEOLOGIC BACKGROUND

The Bishop Tuff is the >600 km^3 (magma volume) product of the 0.765 Ma caldera-forming eruption at Long Valley in eastern California. It is an archetypal example of a compositionally zoned high-silica rhyolitic eruption deposit and one of the most thoroughly studied rhyolitic systems in the world (Hildreth 2004; Hildreth and Wilson 2007). The Bishop Tuff is inferred to have been erupted over a span of about 6 days with proximal outcrops concentrated between the Sierra Nevada and the White Mountains (Wilson and Hildreth 1997). The tuff is made up of plinian fall deposits and ash-flow tuffs (ignimbrites) deposited from ground-hugging pyroclastic flows. The fall deposits, where studied in the near-source area, are divided into units F1-F9, preserved within a ~90° fall envelope east of the caldera, and lack any significant time breaks in their stratigraphy; some early fall units may predate ignimbrite packages, but most are demonstrably concurrent with the emplacement of ignimbrite units (see Figure 1). Based on accidental lithic assemblages in the fall deposits and ignimbrite, the initial vent location is in the southeastern portion of the caldera, and the caldera 'unzipped' along ring fractures from there to subsequent vent locations (Hildreth and Mahood 1986; Wilson and Hildreth 1997). Ig1 units are mostly confined to the east of the caldera rim and made up of crystal-poorer material that is interbedded with fall units F2-F8. Ig2 units are distributed both to the north and east of the caldera and represent the crystal-richer material that is inferred from field relationships to be concurrent with fall unit F9 (Wilson and Hildreth 1997). The Bishop Tuff mineral assemblage consists of quartz, sanidine, plagioclase, biotite, titanomagnetite, ilmenite, zircon, apatite, and allanite (Hildreth

1

1979). Pyroxene (both orth- and clino-) also occurs, but is found only in the later-erupted ignimbrite packages (Ig 2).
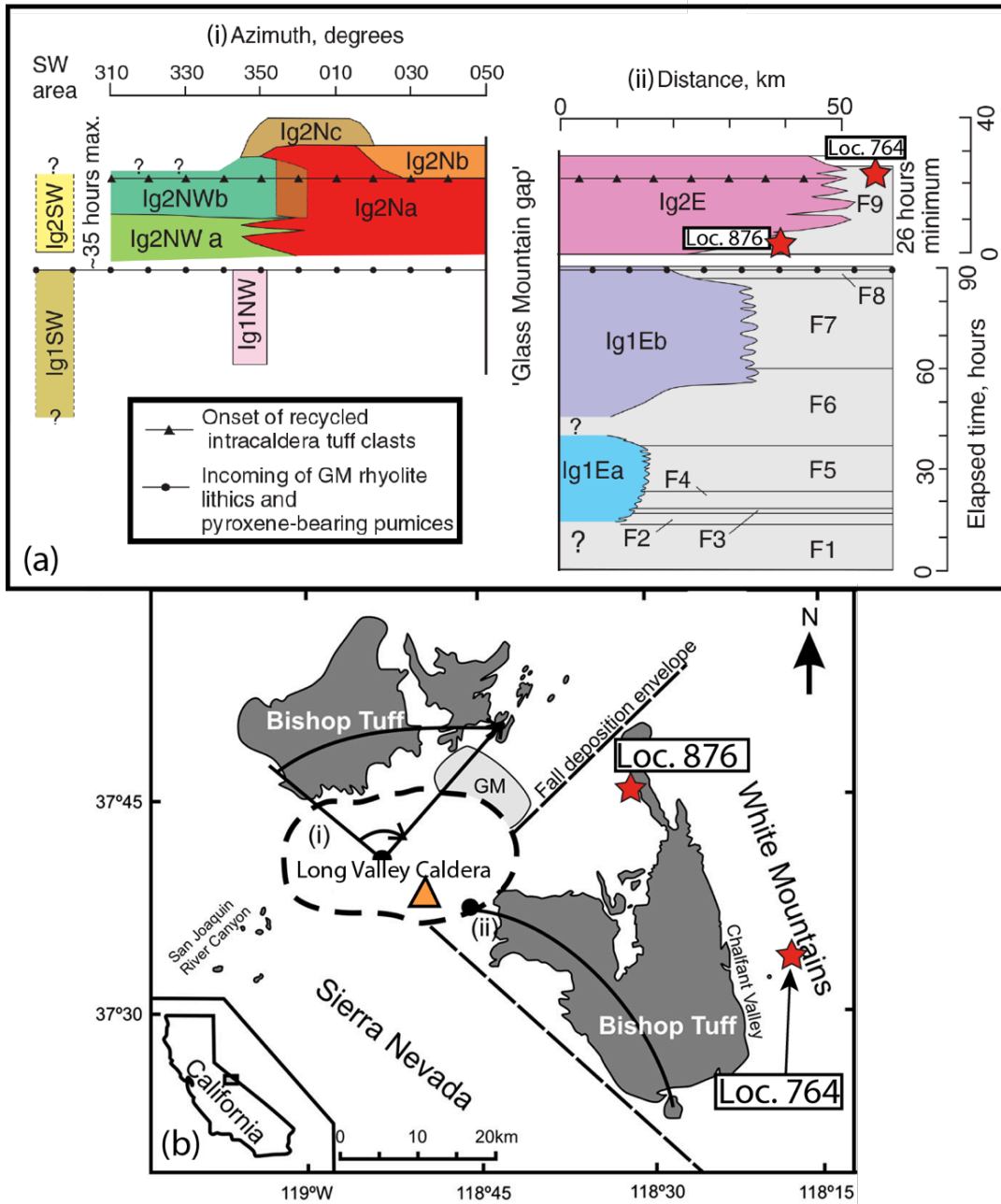
Figure 1. Simplified map and stratigraphy of the Bishop Tuff after Hildreth and Wilson (2007). **a)** Stratigraphy of proximal Bishop Tuff; lines *i* and *ii* in **b** correspond to cross sections of northern and eastern ignimbrite lobes (colored) and plinian fall deposits (grey). Eruption timescales determined by Hildreth and Wilson (2007) are shown to the right of the stratigraphy. **b)** Simplified outline map of Long Valley Caldera (eastern California) and the surrounding Bishop Tuff ignimbrite deposits (gray shading). Dashed line is the caldera outline; orange triangle indicates the initial vent location. Stars signify sample locations within the fall envelope with locality numbers from CJN Wilson (pers. comm.).

Past compositional studies of whole rock, matrix glasses, melt inclusions, phenocrysts and crystal zoning, Fe-Ti oxide thermometry and oxygen isotopes studies all converge on a thermally and compositionally zoned reservoir in the upper crust prior to eruption of a vapor-saturated Bishop Tuff magma (Hildreth 1979; Dunbar and Hervig 1992; Wallace et al. 1999; Bindeman and Valley 2002; Hildreth and Wilson 2007; Ghiorso and Evans 2008; Roberge et al. 2013; Chamberlain et al. 2015; Evans et al. 2016). While the zonation of the Bishop Tuff has been heavily supported (despite alternative interpretations, e.g. Gualda and Ghiorso 2013), the timing of the later portions of the eruption remains enigmatic.

The earliest Bishop deposits represent the most evolved (higher SiO_2) and crystal-poor magma compositions, whereas less evolved, crystal-richer (but still rhyolitic) compositions became more prominent as the eruption progressed, tapping deeper, hotter portions of the magma reservoir. An important point is that the overall compositional zonation in the reservoir was present long before late-stage injections of less evolved/hotter rhyolites that caused variable thicknesses of overgrowths ("bright rims"; expressed as such under cathodoluminescence [CL] or back-scattered electron [BSE] imagery) on some crystal populations. The overall compositional arrangement has been inferred to reflect incremental assembly via the addition of numerous influxes of melt from an underlying pluton-scale crystal mush body, coupled with a lack of convective homogenization prior to eruption (Hildreth 2004; Hildreth and Wilson 2007; Chamberlain et al. 2015; Bachmann and Huber 2016). Stratigraphic controls, along with calculated storage pressures and a ~100°C temperature gradient in the pre-eruptive magma, support the interpretation of the Bishop magma as a gradationally zoned system

3

that extended ~2.7 km vertically (Hildreth 1979; Wallace et al. 1999; Peppard et al. 2001; Hildreth and Wilson 2007; Roberge et al. 2013). Late-stage injections into the system that were richer in Ti, Ba, Sr, and CO_2 caused resorption and overgrowths on existing crystal populations in deeper portions of the magma reservoir that were tapped relatively late in the eruption. The effects of this late-stage injection include zonation in quartz, sanidine, zircon and orthopyroxene (Anderson et al. 2000; Peppard et al. 2001; Wark et al. 2007; Gualda et al. 2012a; Roberge et al. 2013; Chamberlain et al. 2014b, 2015).

Growth rims on quartz phenocrysts are visible in CL images, are Ti richer, and often occur over resorbed cores (e.g. Peppard et al., 2001). The inferred cause of these rims is multiple late-stage influxes of less evolved magmas into parts of the reservoir (Wallace et al. 1999; Peppard et al. 2001; Wark et al. 2007; Roberge et al. 2013; Chamberlain et al. 2014a,b). Besides its ability to capture the presence and timing of magma mixing events via Ti zoning, quartz is also useful in deciphering the history of the Bishop tuff magma because it often incorporates melt inclusions (MIs), which are pockets of pre-eruptive melt trapped during crystal growth. Melt inclusions represent a snapshot of the magma melt composition and volatile content at the time of their entrapment. In contrast, matrix glasses, from quenched glassy pumice and ash, represent magma compositions just prior to eruption and are partly to wholly outgassed (although subsequently often partly rehydrated by meteoric water passing through the deposit).

With continued study, Bishop Tuff deposits are helping us understand how large bodies of magma are stored in the crust and ultimately erupted. A remaining area of uncertainty in the Bishop Tuff, however, is tying together the later stages of ignimbrite activity from vents on the northern and eastern margins of Long Valley caldera with their

coeval F9 fall deposits. In this study, data from 192 quartz-hosted melt inclusions and 40 matrix glass analyses have been collected from samples from two stratigraphically controlled locations of the F9 fall deposits. These data are used along with CL textures of 52 quartz phenocrysts and modeled diffusion timescales of those with bright-CL rims to investigate the timing of magma mixing processes and assess the relative timing of ignimbrite emplacement during later parts of the Bishop Tuff eruption. Melt inclusion and glass trace element concentrations in the F9 samples are compared to previous studies on MIs (Dunbar and Hervig 1992; Wallace et al. 1999; Anderson et al. 2000; Roberge et al. 2013) and matrix glasses (Roberge et al. 2013; Chamberlain et al. 2015) from elsewhere in the Bishop Tuff. Many previous studies (following Hildreth 1979) have referred to eastern crystal-poor deposits as 'early Bishop Tuff' and northern crystal-rich deposits as 'late Bishop Tuff.' Here we confirm that the Bishop Tuff eruption did not happen in two geographically and temporally distinct phases. We therefore abandon the "early" and "late" labels and instead, following Chamberlain et al. (2015), refer to the ignimbrite sectors as eastern (previously "early") and northern (previously "late") ignimbrite lobes. Although Wilson and Hildreth (1997) and Hildreth and Wilson (2007) proposed that the northern and eastern lobes were coevally emplaced on the basis of field relationships, geochemical evidence to support or disprove that hypothesis has hitherto been lacking. The present study provides that geochemical evidence. The timing of later stages of the eruption was realistically more complex than previously assumed, and the large range in compositions and textures within the final fall unit, F9, has helped us determine that many vents around the caldera must have been erupting simultaneously.

CHAPTER II

METHODS

Samples

This study focused exclusively on unit F9, the last fall unit in the Bishop Tuff

sequence. F9 is exposed at multiple locations within the fall deposit envelope, but it is at

all but one locality interrupted and overlain by ignimbrite. The one exception is at a site

(locality 764 of Wilson, pers. Comm.) on the western slopes of the White Mountains east

of Chalfant Valley. Although uplifted by post-Bishop faulting along the western range

front of the White Mountains (e.g. Stockli et al. 2003), it appears that this location was

topographically higher at the time of eruption than the other localities in the Chalfant

Valley because the only ignimbrite present is a ~1 cm veneer deposit. With 205 cm of F9

material exposed, this site provides an opportunity to sample fall material that extends

stratigraphically higher and later than any other Bishop fall section. Stratigraphically

controlled samples were collected from two exposures of F9 fall unit: (1) Locality 764, as

described above, and (2), Locality 876 near the northern end of the east ignimbrite lobe

where ~90 cm of more proximal F9 material is preserved (Figure 1). Matrix glasses and

192 melt inclusions from four layers within F9 at location 764 and one layer in the center

of F9 at location 876 were analyzed for major elements by electron microprobe (EPMA)

and trace elements using laser ablation inductively coupled plasma mass spectrometry

(LA-ICP-MS). Prior to EPMA and LA-ICP-MS analysis, 38 of the MIs were analyzed for

H_2O and CO_2 by Fourier transform infrared spectroscopy (FTIR). In the Bishop system,

melt inclusions are considered reliable recorders of melt composition at the time of

entrapment as indicated by the similarities between MI and matrix glass trace element

6

compositions and findings that boundary layer effects during trapping are negligible (Anderson 1991; Dunbar and Hervig 1992; Lu et al. 1992)

Sample preparation

Bulk fall deposit samples from layers within F9 were sieved, and quartz grains from the 500 to 1400 µm sieve fractions were picked out and viewed in isopropyl alcohol, which has a similar refractive index to quartz, to select those grains that contained one or more melt inclusions larger than ~50 µm. Melt inclusions larger than ~50 µm were preferred to ensure that the interiors of inclusions could be analyzed such that the data are not affected by any potential boundary layer effects at the wall of the inclusion (Lu et al. 1992). Larger MI also ensure microprobe analyses excite only the MI glass and no surrounding quartz. Grains were picked with evidence of glass selvedges to ensure quartz crystals are juvenile Bishop material and not inherited from older Glass Mountain material. No MIs in this study contain evidence such as vapor bubbles or microlites for slow cooling or post-entrapment crystallization (as described in Wallace et al. 2003). For those MIs being prepared for FTIR analysis, the host quartz was mounted on a glass slide with acetone-soluble Crystalbond™ adhesive and polished down to a 1-µm grit size on both sides of the melt inclusion to make a wafer that intersected the same inclusion on both sides (doubly intersected). After FTIR analysis, the doubly intersected wafers and other singly intersected MIs in their quartz hosts were mounted in 1-inch epoxy rounds to be analyzed by EPMA and LA-ICP-MS. For matrix glass analyses, loose pumice fragments from F9 were vacuum impregnated with epoxy and polished to a 1-µm grit size after mounting in 1-inch rounds.

Analytical techniques

H₂O and CO₂ in doubly intersected melt inclusions were analyzed using a Thermo Nicolet Nexus 670 Fourier transform infrared (FTIR) spectrometer interfaced with a Continuum IR microscope at the University of Oregon. Absorbance of molecular H_2O (5200 cm⁻¹), OH⁻ groups (4500 cm⁻¹), and molecular CO_2 (2350 cm⁻¹) were measured as peak heights. Peak heights were calculated using a straight line background correction (Dixon and Holloway 1995). Total dissolved H_2O (molecular H_2O plus OH⁻) and CO_2 were calculated using the Beer-Lambert Law:

$$c = \frac{M \cdot A}{\rho \cdot t \cdot \epsilon}$$

where c is the concentration (weight fraction) of the absorbing species, M is the molecular weight of H_2O species (18.02) or CO_2 (44.00), A is the absorbance intensity, ρ is the room temperature density of rhyolite glass, t is the inclusion thickness in μm, and ε is the molar absorption coefficient. The molar absorption coefficients vary with total H_2O content for water species in rhyolite glass, thus we use the Beer's Law algorithm of Zhang et al. (1997) to calculate total H_2O. The effect of H_2O content on room temperature glass densities was calculated using $\rho/\rho_0 \approx 1\text{-}C$, where C is the mass fraction of water (from Zhang et al. 1997). A gas-shielding cup was placed over the sample and was purged with CO_2-free air to mitigate atmospheric CO_2 contamination. Melt inclusion thicknesses were measured via three different methods: 1) focusing on a calibrated optical microscope using the equation, $d = d' \frac{n_o}{n_i}$, where d is the true depth/thickness, d' is the measured depth, n_o is the refractive index of the medium (~1.554 for quartz), and n_i is the refractive index of air (~1.0003 at room temperature); 2) using a digital micrometer (±2 μm); 3) using the reflectance interference fringe method (Wysoczanski and Tani

8

2006; Nichols and Wysoczanski 2007). The average of the two methods with the most similar measurements was used for each inclusion with differences in measurements between them no greater than ±5 μm. Based on three replicate analyses, estimated precisions (2σ) are <3% for total H_2O and <6% for CO_2.

Major element concentrations for melt inclusions and matrix glasses were determined using a Cameca SX-100 electron microprobe (EPMA) at the University of Oregon. Operating conditions were as follows: 15 kV and 10 nA for Si, Ca, Na, Fe, Al, and K, and 50 nA for Cl, F, Mg, and Ti. 5-10 μm spot sizes were used for all analyses. Na, K, Si, and Al concentrations were calculated via the time dependent intensity correction in Probe for Windows (Donovan et al. 2007). Melt inclusions and matrix glasses were then analyzed for trace elements by LA-ICP-MS at Oregon State University using 40-50 μm spot sizes depending on the size of the melt inclusion or region of solid glass within pumice pieces. Four glasses were used as secondary standards (ATHO-1G, T-1G, BHVO-2G, and BCR-2G), and GSE-1G was the calibration standard (Jochum et al. 2005, 2006). Trace element abundances were normalized to [29]Si from EPMA analyses.

Cathodoluminescence (CL) images of 52 F9 quartz crystals (Figure 2) were obtained with a FEI Quanta 200 ESEM microscope at 20 kV and 5 μm spot sizes also at the University of Oregon. CL intensity variations within quartz crystals are generally inferred to be caused by changes in Ti content, with higher Ti zones appearing brighter in greyscale (Wark and Watson 2006; Wark et al. 2007; Matthews et al. 2012a, b).

Diffusion modeling

Grayscale profiles of Ti in quartz were extracted from CL images using ImageJ® software. We assume profiles of zoning textures were initially sharp step functions,

9

because in many cases the older crystal core has been partially resorbed, providing a sharp intitial boundary for overgrowth. A simple 1D model was used to solve the diffusion equation for Ti in quartz. Model parameters used are as follows: $D_0 = 7x10^{-8}$ (ms^{-2}); $E_{act} = 273,000$ (J/mol); $T = 780$ ˚C; no compositional or oxygen fugacity dependence (Cherniak et al. 2007; Hildreth and Wilson 2007; Chamberlain et al. 2014a). We use a temperature of 780˚ C because this was the inferred temperature for the deeper parts of the Bishop magma body prior to the influxes of the Ti-richer, slightly hotter melt (Chamberlain et al. 2014a). The diffusivity is expressed as:

$$D = D_0 e^{\left(\frac{-E}{RT}\right)},$$

where D_0 is the diffusion coefficient for Ti at infinite temperature, E is the activation energy, R is the gas constant, and T is the temperature in Kelvins. The diffusion equation assuming constant diffusivity is:

$$\frac{dC}{dt} = D \frac{d^2C}{dx^2} .$$

To determine the best-fit timescales and associated errors, we use a chi-squared criterion to quantify the goodness-of-fit. The formula for chi-squared (x^2) compares observed (model, O) and expected values (measured data, E):

$$x^2 = \sum \frac{(O-E)^2}{E} .$$

Lower chi-squared numbers correspond to better fit. Reported uncertainties for each timescale were found based on the chi-squared criterion and take into account temperature uncertainties of Fe-Ti oxide thermometry (Hildreth and Wilson 2007) and two-feldspar thermometry (Chamberlain et al. 2014a).

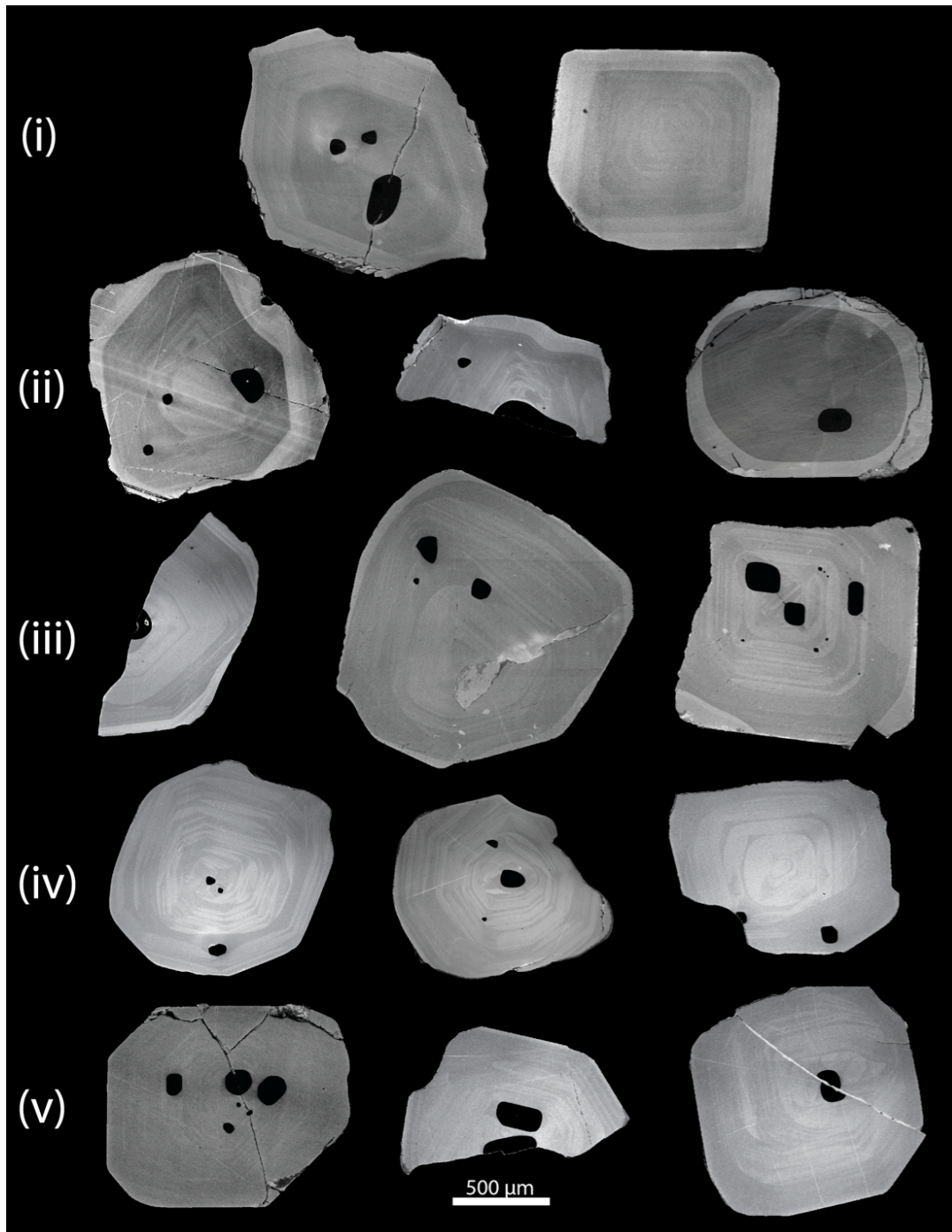**Figure 2.** Representative CL textures of F9 quartz phenocrysts organized into general textural groups by row. (i) quartz with multiple bright zones at the rim of the crystal with euhedral cores, (ii) quartz with thick bright rims over resorbed cores, (iii) quartz with thin and/or incomplete bright rims and partially resorbed cores, (iv & v) quartz lacking bright rims but containing varying extents of interior oscillatory zoning.

CHAPTER III

RESULTS

Quartz CL textures

All 52 imaged F9 quartz crystals exhibit CL zoning, although it is more subtle in some (see Figure 2). Nearly all internal zoning consists of alternating brighter and darker bands as the crystals grew outwards from their cores (Peppard et al. 2001; Wark and Watson 2006; Wark et al. 2007). F9 quartz crystals fall largely into five textural groups corresponding to rows *i-v* in Figure 2: *i*) darker cores transitioning out to multiple brightening zones towards the rims; *ii*) thick bright rims surrounding darker rounded/resorbed cores; iii) thin or discontinuous bright rims surrounding darker partially rounded/resorbed cores; *iv*) internal oscillatory zoning with high contrast that gets slightly darker towards rims; and *v*) faint oscillatory zoning with no significant change in CL intensity from core to rim. Overall, ~40% of F9 quartz crystals have bright rims, leaving the remaining ~60% without bright rims. Over 50% of F9 melt inclusions that were analyzed occur near crystal cores, with >40% located about halfway between cores and edges, and ~5% located in darker edge regions (all in textural group iv). No melt inclusions trapped within bright rim zones were observed in the F9 crystals studied here.

Ti-in-quartz diffusion modeling

Twelve of the 52 imaged F9 quartz crystals had bright-CL rims with enough contrast and high enough image resolution to model. Interior oscillatory zoning was not considered in this study (see Gualda et al. 2012b) but could be used in future studies (cf. Petrone et al. 2016). Over 50 profiles were modeled from the 12 quartz grains (e.g. Figure 3). The longest modeled timescale is 83 years (+40/-30 years), and the shortest

timescale is 15 years (+10/-5 years). One timescale of 310 years (±100 years) was found

from the boundary between an inner thick bright-CL zone and dark core (the first quartz

in row *I* of Figure 2), but the thinner, outermost brighter rim zone of the same crystal

gave a timescale of 19 years (+15/-10 years). The average timescale from the outermost

bright-CL rims in unit F9 is 33 years (±20 years). All reported timescales (see Figure 8)

are maxima because we assume profiles are perpendicular to boundaries and that there is

an initial sharp step function (Costa and Morgan 2010; Matthews et al. 2012a).
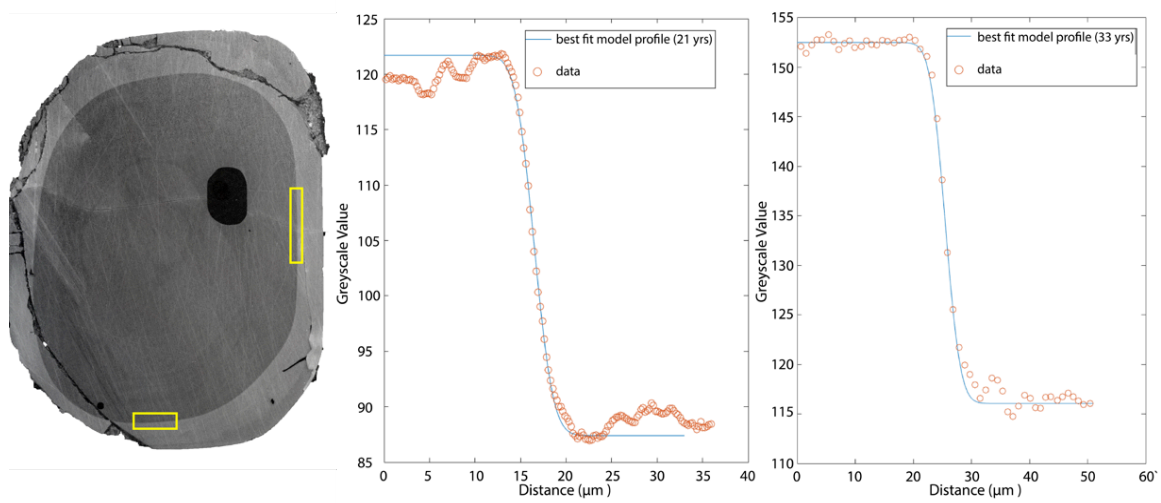
Figure 3. CL image of a representative F9 quartz crystal (internal MI was analyzed as BP141-E-MI1) with a thick bright rim overgrowth and profiles across the boundary between its rim and core to the right. The yellow boxes represent areas over which multiple transects were made and collapsed into single curves. Orange circles are measured data, blue lines are the best-fit models, the x-axes are the distances across each profile, and the y-axes are greyscale values. Similar timescales (within error) from both shown profiles indicate that the profiles are consistent regardless of crystal axis.

Compositional variations in F9 melt inclusions and host matrix glasses

Quartz-hosted MIs and matrix glasses analyzed here from fall unit F9 at location

764 have average SiO_2 contents of 76.3 wt.% and 76.6 wt.% respectively, well within the

range for high-silica rhyolites and similar to the pumice, MI, and matrix glass

compositions reported in Wallace et al. (1999), Hildreth and Wilson (2007), and

Chamberlain et al. (2015). Location 876 MIs produce an average F9 SiO_2 content of 75.8

wt.%. Normalized Qtz, Ab, and Or contents of F9 MI and matrix glasses are plotted over

data fields for eastern and northern ignimbrite MI compositions on a Qtz-Ab-Or ternary

diagram in Figure 4. Values are corrected for anorthite content using the equations from

Blundy and Cashman (2001) because An is not accounted for in the haplogranitic

projection. The majority of F9 melt inclusions fall between the 100 and 300 MPa cotectic

curves and overlap onto both eastern and northern melt inclusion compositional fields

based on previously published data.
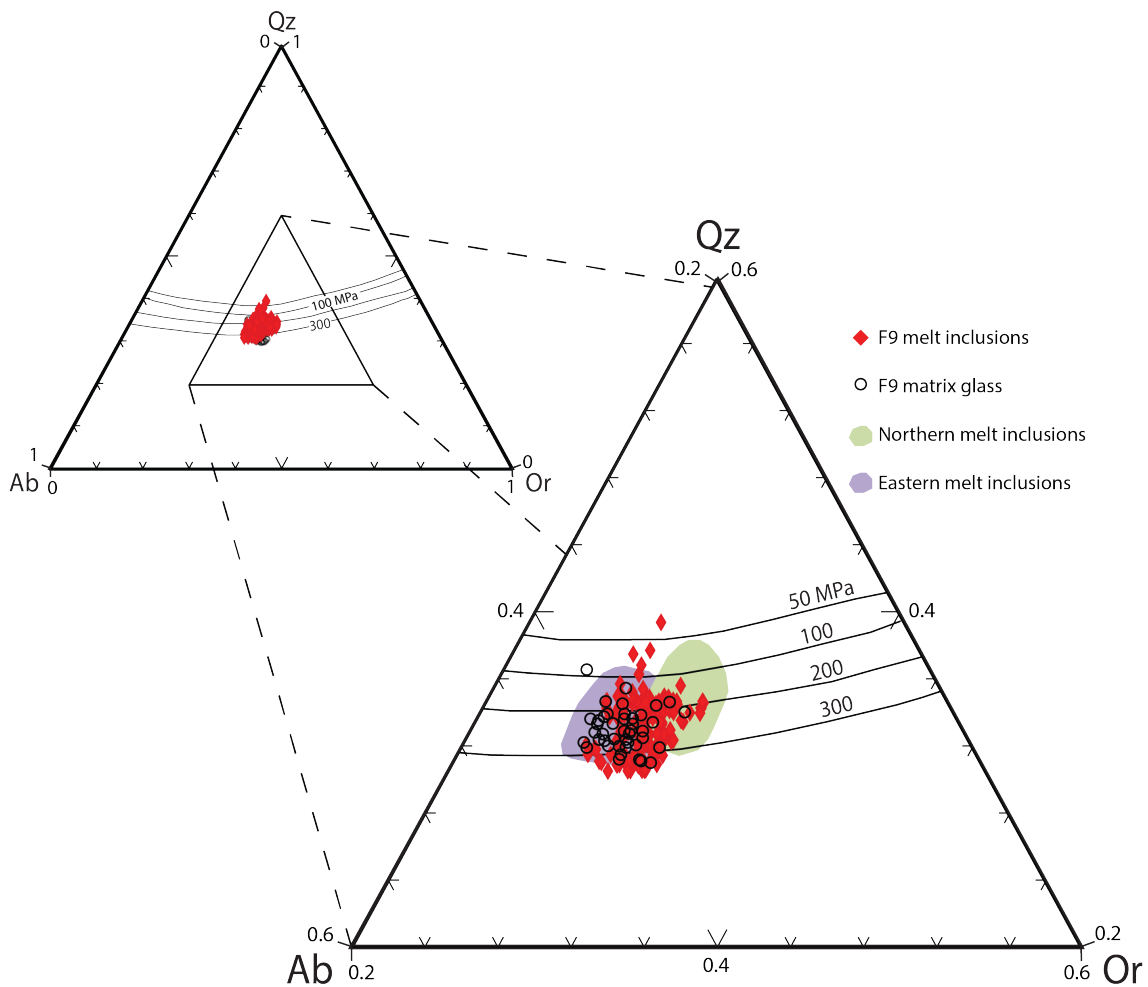
Figure 4. Projection of F9 quartz-hosted melt inclusion (MI) and host matrix glass compositions onto the haplogranitic Qtz-Ab-Or ternary system. Qtz-Ab-Or proportions were calculated on the basis of CIPW normalization and corrected for anorthite content using the method of Blundy and Cashman (2001). Purple and green fields represent quartz-hosted MIs from Ig2 eastern and northern ignimbrite lobes respectively (data from Wallace et al. 1999). The majority of data points fall within the range defined by the 50 and 300 MPa cotectic curves (see also Gualda and Ghiorso 2013).

Despite the limited major element variations, trace element abundances vary widely throughout the Bishop Tuff and even within the MI population from F9. In the Bishop Tuff system, Nb, Rb, and Y were shown to be the most incompatible elements during differentiation, whereas Sr, Ba, La, and Ce were the most compatible (Hildreth 1979; Michael 1983; Lu et al. 1992). These inferences are supported by element plots in Figure 5 of F9 MIs as well as more recent published data from the rest of the eruptive stratigraphy (e.g. Roberge et al. 2013). Rb and Nb increase with progressive fractional crystallization, whereas Ce decreases as it is taken up into minerals like apatite and allanite, thus confirming the compatible behavior of Ce in the Bishop system. Given the incompatibility of Nb and Rb and compatible behavior of Ce, the ratios Nb/Ce and Rb/Ce provide useful indicators of differentiation in the crystallizing magma reservoir (Roberge et al. 2013), as shown in Table 1 and Figure 6. Melt inclusions from the four sampled layers within F9 at Loc. 764 span a large range in the two ratios, covering nearly the entire previously published range for Bishop Tuff MI compositions. Most analysed F9 matrix glasses are similarly or slightly more evolved than their corresponding MIs with the exception of a few glass values 141 cm from the base of F9 at location 746 (middle panel of Figure 6). Any matrix glass analyses that fell off of the fractionation trends between Nb versus Sr/Rb and Ba/Rb may have hit small groundmass feldspars and were therefore removed from our dataset. F9 MI compositions follow fractionation trends for most other trace elements, overlapping with published values for MIs from both eastern and northern ignimbrite lobes (Chamberlain et al. 2015). All analyzed melt inclusions from Loc. 876 plot towards the most evolved end of the F9 trace elemental spectrum and overlap with the center of the eastern matrix glass field in Figure 5.

15

Table 1. FTIR data for F9 melt inclusions and trace element ratios of F9 melt inclusions and matrix glasses

Sample name	Type	Location	H_2O wt.%	CO_2 ppm	Nb/Ce	Rb/Ce
F9BP147_MI1	MI	764	4.18	150	0.56	4.12
F9BP147_MI2a	MI	764	5.47	100	0.66	4.85
F9BP147_MI2b	MI	764	4.96	69	0.64	4.53
F9BP147_MI2c	MI	764	4.96	69	0.58	4.46
F9BP147_MI3a	MI	764	5.80	39	0.84	5.73
F9BP147_MI3b	MI	764	4.77	29	0.77	5.07
F9BP147_MI3c	MI	764	5.22	30	0.71	5.13
F9BP147_MI4	MI	764			0.64	4.74
F9BP147_MI4b	MI	764			0.67	4.76
F9BP147_MI5	MI	764	4.26	88	0.54	3.99
F9BP147_MI6a	MI	764	5.84	56	0.66	5.21
F9BP147_MI6b	MI	764	5.50	47	0.69	5.28
F9BP147_MI8	MI	764	4.28	528	0.35	2.25
F9BP143_MI1	MI	764	5.42	62	0.64	5.81
F9BP143_MI2a	MI	764	4.98	113	0.54	4.30
F9BP143_MI2b	MI	764	4.54	258	0.54	4.10
F9BP141_MI1	MI	764	4.73	86	0.59	5.10
F9BP141_MI2	MI	764	4.33	62	0.59	5.10
F9BP138_MI1	MI	764	4.34	61	0.61	5.25
F9BP143_MI3	MI	764	5.57	79	0.56	4.07
F9BP141_MI3	MI	764	5.24	50	0.57	3.91
F9BP141_MI3b	MI	764	5.48	103	0.54	3.92
F9BP141_MI4	MI	764	4.23	373	0.40	2.82
F9BP138_MI2	MI	764	5.58	41	0.49	3.58
F9AFBP138_MI3	MI	764	4.94	112		
F9AFBP138_MI4a	MI	764	3.72	34	0.54	3.95
F9AFBP138_MI4b	MI	764			0.54	4.03
F9AFBP138_MI5a	MI	764	4.80	22	0.64	4.63
F9AFBP138_MI5b	MI	764			0.60	4.95
F9AFBP138_MI6a	MI	764	2.80	112	0.60	4.04
F9AFBP138_MI6b	MI	764	3.82	36	0.59	4.47
F9AFBP138_MI6c	MI	764			0.56	3.76
F9AFBP138_MI7a	MI	764	3.99	158	0.45	3.31
F9AFBP138_MI7b	MI	764	4.86	156	0.49	3.86
F9AFBP138_MI7c	MI	764			0.48	3.53
F9AFBP138_MI8	MI	764	4.43	96	0.53	3.86
F9AFBP141_MI5a	MI	764	4.51	60	0.54	3.84
F9AFBP141_MI5b	MI	764			0.52	3.68
F9AFBP141_MI6	MI	764	4.12	93	0.49	3.54
F9AFBP143_MI4	MI	764	3.85	456	0.21	1.75

Table 1. Continued

Sample name	Type	Location	H_2O wt.%	CO_2 ppm	Nb/Ce	Rb/Ce
F9AFBP138_MI9	MI	764	5.15	54	0.62	4.49
F9AFBP138_MI9b	MI	764			0.52	3.80
F9AFBP143_MI5	MI	764	4.69	59	0.61	4.70
F9AFBP143_MI6a	MI	764	4.55	191	0.47	3.60
F9AFBP143_MI6b	MI	764	4.97	57	0.55	3.90
F9AFBP141_MI7	MI	764	4.36	91	0.53	3.86
BP138-A-MI1	MI	764			0.54	3.62
BP138-B-MI1	MI	764			0.59	4.12
BP138-C-MI1	MI	764			0.56	4.11
BP138-C-MI2	MI	764			0.55	3.65
BP138-D-MI1	MI	764			0.64	4.43
BP138-F-MI1	MI	764			0.61	4.30
BP138-F-MI2	MI	764			0.63	4.28
BP138-G-MI1	MI	764			0.52	3.31
BP138-H-MI1	MI	764			0.61	4.22
BP138-H-MI2	MI	764			0.56	3.86
BP138-I-MI1	MI	764			0.59	3.76
BP138-I-MI2	MI	764			0.74	5.56
BP138-J	MI	764			0.53	4.09
BP138-K-MI1	MI	764			0.62	4.34
BP138-K-MI2	MI	764			0.59	4.34
BP138-L-MI1	MI	764			0.67	4.71
BP138-L-MI2	MI	764			0.72	5.55
BP138-M-MI1	MI	764			0.53	4.16
BP138-M-MI2	MI	764			0.54	3.74
BP138-M-MI3	MI	764			0.52	3.87
BP138-N-MI1	MI	764			0.53	4.72
BP138-N-MI3	MI	764			0.58	4.09
BP138-O-MI2	MI	764			0.54	4.01
BP138-O-MI3	MI	764			0.63	4.82
BP138-P-1	MI	764			0.68	5.45
BP138-P-2	MI	764			0.63	4.72
BP138-Q-1	MI	764			0.55	4.18
BP138-R-1	MI	764			0.56	3.66
BP138-R-2	MI	764			0.56	3.78
BP138-T-MI1	MI	764			0.56	4.06
BP138-T-MI3	MI	764			0.61	4.56
BP138-U-MI1	MI	764			0.53	4.17
BP138-U-MI2	MI	764			0.49	3.62
BP138-V-MI2	MI	764			0.59	4.67
BP138-W-MI1	MI	764			0.54	4.39

Table 1. Continued

Sample name	Type	Location	H$_2$O wt.%	CO$_2$ ppm	Nb/Ce	Rb/Ce
BP138-X-MI2	MI	764			0.61	4.46
BP138-X-MI3	MI	764			0.73	5.83
BP138-Y-MI1	MI	764			0.66	4.54
BP138-AA-MI1	MI	764			0.55	4.16
BP138-CC-MI1	MI	764			0.59	4.31
BP138-EE-MI1	MI	764			0.37	3.40
BP143-A-MI1	MI	764			0.55	3.53
BP143-A-MI2	MI	764			0.52	3.91
BP143-B-MI1	MI	764			0.38	3.14
BP143-C-MI1	MI	764			0.48	3.69
BP143-D-MI1	MI	764			0.54	4.09
BP143-D-MI2	MI	764			0.47	4.04
BP143-E-MI3	MI	764			0.53	4.31
BP143-E-MI5	MI	764			0.56	4.27
BP143-F-MI2	MI	764			0.35	2.80
BP143-G-MI1	MI	764			0.67	4.77
BP143-G-MI2	MI	764			0.65	5.27
BP143-H-MI1	MI	764			0.56	5.02
BP143-I-MI1	MI	764			0.45	3.58
BP143-J-MI1	MI	764			0.59	4.38
BP143-J-MI2	MI	764			0.56	3.91
BP143-K-MI1	MI	764			0.59	4.20
BP143-K-MI2	MI	764			0.57	4.34
BP143-L-MI1	MI	764			0.57	4.38
BP143-M-MI1	MI	764			0.54	4.16
BP143-N-MI1	MI	764			0.60	5.45
BP143-N-MI2	MI	764			0.63	4.86
BP143-O-MI1	MI	764			0.59	4.31
BP143-P-MI1	MI	764			0.39	3.38
BP143-Q-MI1	MI	764			0.54	4.23
BP143-Q-MI2	MI	764			0.64	5.76
BP143-R-MI1	MI	764			0.58	4.59
BP141-A-MI1	MI	764			0.52	3.95
BP141-B-MI1	MI	764			0.53	3.61
BP141-C-MI1	MI	764			0.21	1.59
BP141-C-MI3	MI	764			0.21	1.68
BP141-D-MI1	MI	764			0.57	4.80
BP141-E-MI1	MI	764			0.53	3.59
BP141-G-MI1	MI	764			0.78	5.32
BP141-G-MI2	MI	764			0.68	4.60
BP141-H-MI1	MI	764			0.59	4.62

Table 1. Continued

Sample name	Type	Location	H_2O wt.%	CO_2 ppm	Nb/Ce	Rb/Ce
BP141-I-MI1	MI	764			0.34	2.62
BP141-I-MI2	MI	764			0.27	1.98
BP141-J-MI1	MI	764			0.59	4.60
BP141-J-MI2	MI	764			0.59	4.46
BP141-J-MI3	MI	764			0.65	4.89
BP141-K-MI1	MI	764			0.34	2.92
BP141-L-MI1	MI	764			0.37	2.63
BP141-L-MI2	MI	764			0.46	3.28
BP141-M-MI1	MI	764			0.58	4.30
BP141-O-MI1	MI	764			0.67	5.06
BP141-P-MI1	MI	764			0.50	3.90
BP141-P-MI3	MI	764			0.47	3.83
BP141-Q-MI1	MI	764			0.54	3.92
BP141-Q-MI2	MI	764			0.56	4.46
BP141-S-MI2	MI	764			0.63	5.00
BP141-T-MI1	MI	764			0.82	5.30
BP141-U-MI1	MI	764			0.32	2.44
BP141-U-MI2	MI	764			0.63	4.90
BP141R-A1	MI	764			0.60	5.16
BP141R-B1	MI	764			0.71	5.10
BP141R-D1	MI	764			0.38	3.46
BP141R-E1	MI	764			0.54	4.53
BP141R-G2	MI	764			0.17	1.77
BP141R-H1	MI	764			0.46	4.24
F9BP147-1_MI1E	MI	764			0.48	3.76
F9BP147-2_MI1	MI	764			0.51	3.92
F9BP147-2_MI2E	MI	764			0.52	3.92
F9BP147-3_MI1E	MI	764			0.69	5.22
F9BP147-4_MI1E	MI	764			0.69	4.67
F9BP147-4_MI2	MI	764			0.69	4.97
F9BP147-5_MI1E	MI	764			0.44	3.32
F9BP147-6_MI1	MI	764			0.57	4.57
F9BP147-6_MI2	MI	764			0.55	4.55
F9BP147-6_MI3E	MI	764			0.49	4.08
F9BP147-7_MI1	MI	764			0.57	4.44
F9BP147-7_MI2	MI	764			0.57	4.19
F9BP147-8_MI1	MI	764			0.37	3.18
F9BP147-9_MI1	MI	764			0.54	4.00
F9BP147-9_MI2	MI	764			0.60	4.30
F9BP147-10_MI1	MI	764			0.48	4.40
F9BP147-11_MI1	MI	764			0.50	3.93

Table 1. Continued

Sample name	Type	Location	H_2O wt.%	CO_2 ppm	Nb/Ce	Rb/Ce
F9BP147-12-MI1	MI	764			0.61	3.84
F9BP147-13_MI1E	MI	764			0.53	4.24
F9BP147-13_MI3	MI	764			0.55	4.75
F9BP147-14_MI1	MI	764			0.58	4.39
F9BP147-15_MI1	MI	764			0.56	4.20
F9BP147-16_MI1	MI	764			0.42	3.80
F9BP147-17_MI1	MI	764			0.55	4.86
F9BP147-17_MI2	MI	764			0.64	4.38
BP876-2C1	MI	876			0.52	4.07
BP876-2C3	MI	876			0.53	4.33
BP876-2F1	MI	876			0.54	5.28
BP876-2H1	MI	876			0.56	4.46
BP876-2I1	MI	876			0.54	4.52
BP876-2L2	MI	876			0.53	4.32
BP876-2M2	MI	876			0.48	4.71
BP876-2N2	MI	876			0.50	4.02
BP876-2Q1	MI	876			0.50	4.53
BP876-2R1	MI	876			0.54	4.49
BP876-2U1	MI	876			0.49	4.32
BP876-2V1	MI	876			0.44	3.67
BP876-2W1	MI	876			0.48	4.42
BP876-2Y1	MI	876			0.49	4.26
BP876-2Z1	MI	876			0.63	4.70
BP876-2AA1	MI	876			0.52	4.54
BP876-2BB1	MI	876			0.52	4.44
BP876-2CC1	MI	876			0.58	4.76
BP876-2FF1	MI	876			0.64	5.31
BP876-2FF2	MI	876			0.58	5.10
BP141R-1	matrix	764			0.40	3.12
BP141R-3	matrix	764			0.35	2.55
BP141R-4a	matrix	764			0.79	3.95
BP141R-4b	matrix	764			0.80	5.55
BP141R-5	matrix	764			0.88	5.14
BP141R-6a	matrix	764			0.80	4.97
BP141R-7a	matrix	764			0.71	5.30
BP141R-9b	matrix	764			0.85	5.52
BP141R-11	matrix	764			0.82	5.47
BP141R-12a	matrix	764			0.82	5.31
BP141R-12b	matrix	764			0.72	5.46
BP141R-13a	matrix	764			0.75	5.67
BP141R-13b	matrix	764			0.76	5.15

Table 1. Continued

| Sample name	Type	Location	H_2O wt.%	CO_2 ppm	Nb/Ce	Rb/Ce
BP141R-14	matrix	764			0.75	5.39
BP141R-15	matrix	764			0.77	5.21
BP141R-16	matrix	764			0.82	5.13
BP141R-18	matrix	764			0.34	2.24
BP147-1a	matrix	764			0.75	4.75
BP147-1b	matrix	764			0.76	4.93
BP147-2	matrix	764			0.75	4.68
BP147-4	matrix	764			0.75	4.70
BP147-5a	matrix	764			0.72	4.90
BP147-5b	matrix	764			0.79	4.81
BP147-7c	matrix	764			0.78	5.57
BP147-8	matrix	764			0.77	4.96
BP147-11a	matrix	764			0.71	4.81
BP147-11b	matrix	764			0.73	5.02
BP147-12a	matrix	764			0.74	4.66
BP147-12b	matrix	764			0.75	5.19
BP147-13a	matrix	764			0.75	5.17
BP147-13b	matrix	764			0.81	4.67
BP147-14	matrix	764			0.71	4.35
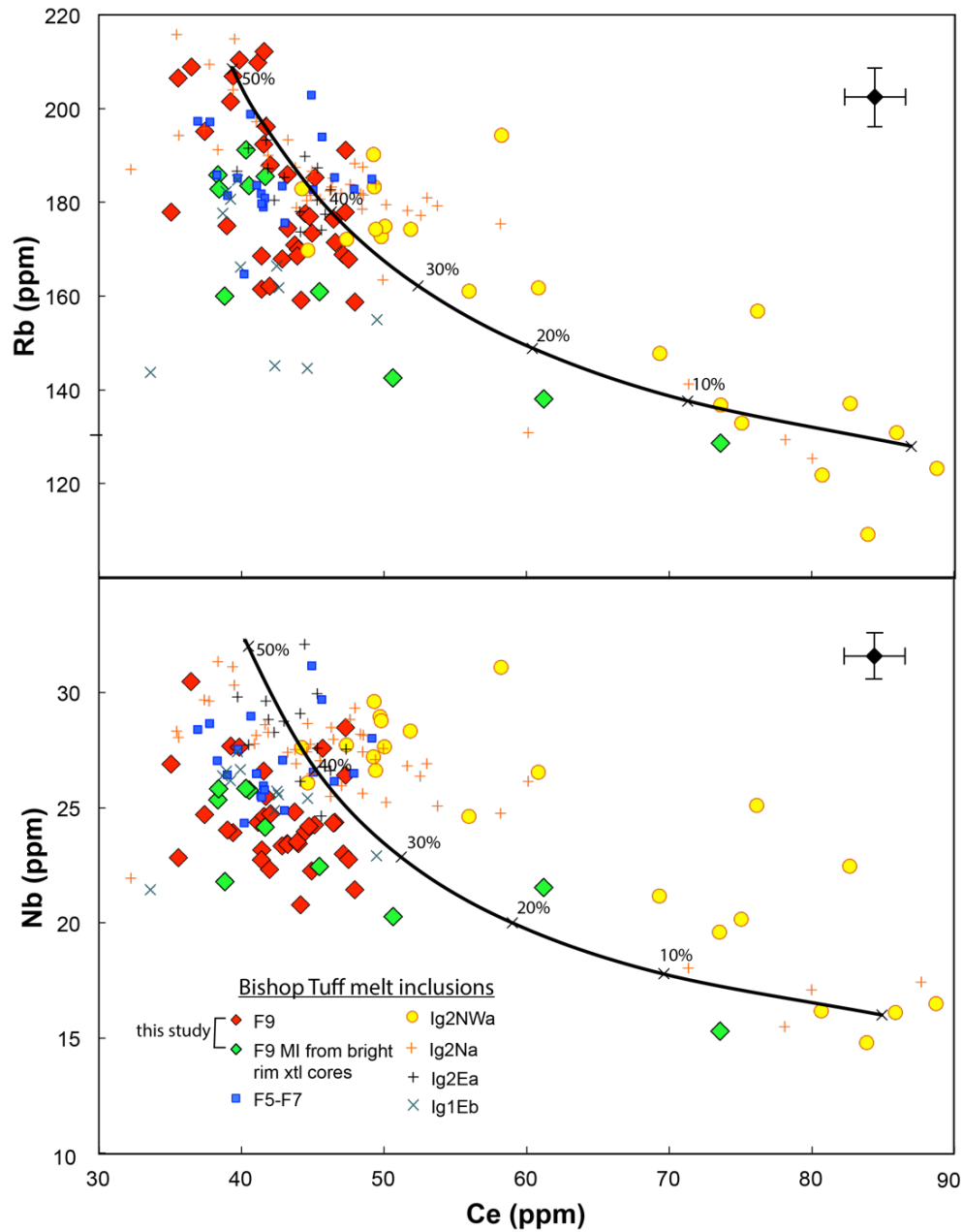
Figure 5. Rb, Nb, and Ce concentrations for a spectrum of Bishop Tuff quartz-hosted melt inclusions (data from Wallace et al. 1999 and Roberge et al. 2013). Melt inclusions from fall unit F9 are shown as diamonds with green diamonds indicating MI within quartz with confirmed bright rims. Solid black lines represent equilibrium crystallization trends calculated with starting compositions approximating the least evolved Bishop melt inclusions using the following bulk partition coefficients (D): D = 0.0298 for Rb, D = 0 for Nb (from Roberge et al. 2013), and D = 3.2 for Ce (modified from Lu et al. 1992). Rb and Nb were incompatible in the Bishop Tuff magma, while Ce was compatible. The crystallization trends illustrate their different compatibilities during fractional crystallization. Error bars are based on average 1 SE analytical uncertainties at the relevant concentrations.
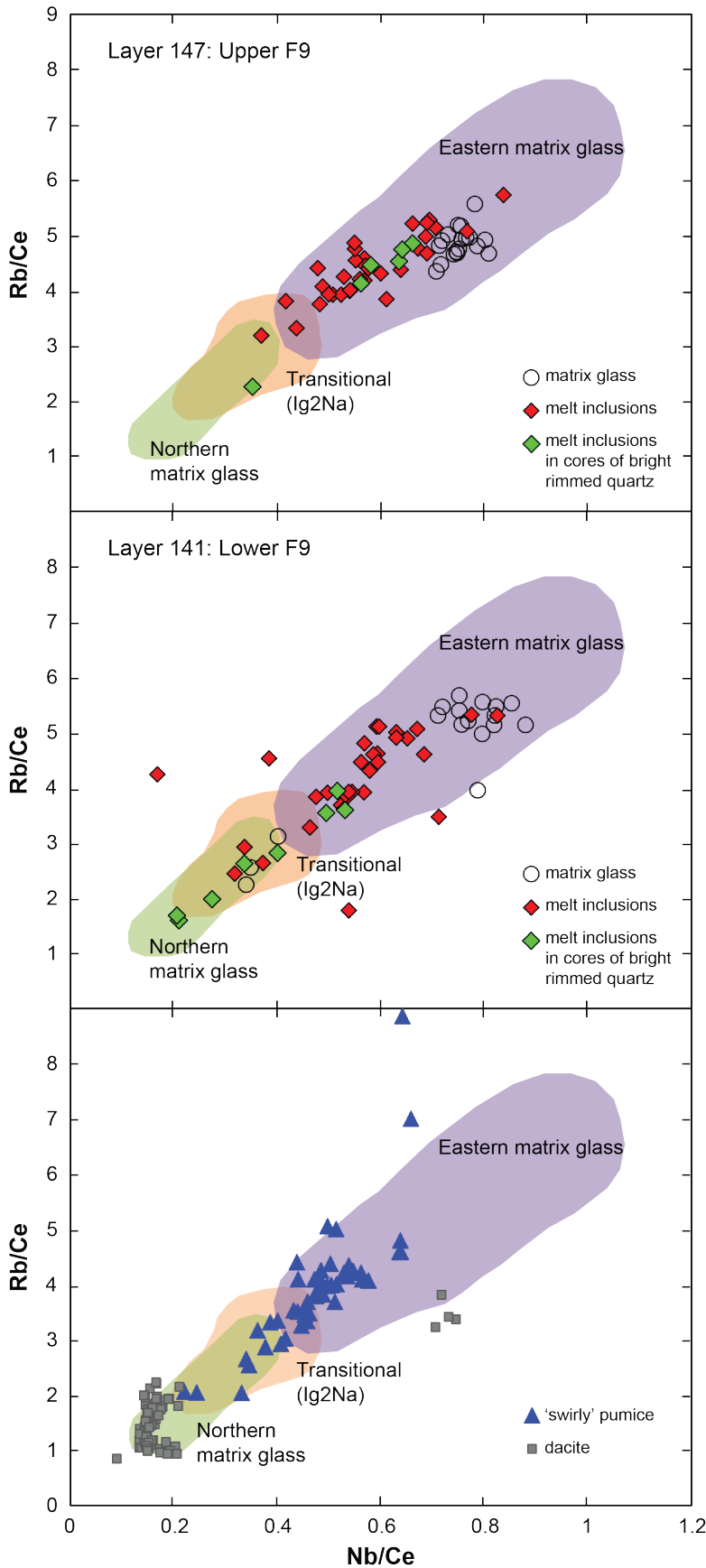
Figure 6. Trace element ratios Rb/Ce and Nb/Ce for MI and matrix glasses from fall unit F9 as well as swirly pumice from later (Ig2) eastern and northern ignimbrite lobes and dacite clasts from Ig2NWa (bottom plot). As in Fig. 5, MIs from bright rim F9 quartz crystals are shown as green diamonds. The upper two plots represent two different layers within the 2.05 m exposure of F9 at location 764. Colored fields are matrix glass ranges from Chamberlain et al. (2015) for the eastern (purple) and northern (green) ignimbrite lobes as well as a separate field for Ig2Na (orange), which has a transitional trace element chemistry between the eastern and other northern Ig2 packages.

Volatile abundances in F9 MIs

The dissolved volatile concentrations in F9 MIs are presented in Table 1 and Figure 7. They range from 3.7-5.8 ± 0.3 wt.% H_2O (ignoring a low H_2O outlier) and from 22-530 ± 25 ppm CO_2. Volatiles were measured only for MI from Loc. 746 and none analyzed from Loc. 876. Melt inclusions with the highest H_2O values overlap with the high-H_2O and low-CO_2 values previously reported from the eastern Ig2 ignimbrite (Wallace et al. 1999). Melt inclusions with the highest CO_2 concentrations come from the cores of quartz crystals with bright CL rims and fall within the range of values from the crystal-rich northern ignimbrite (Wallace et al. 1999; Roberge et al. 2013). However, there is a significant subset of F9 MIs that have both low water and low CO_2 concentrations. These values occur in both cores of crystals with bright rims (3 of 38 MIs measured for volatiles) and the cores and edges of many crystals without bright rims (10 of the 38 MI). There is more scatter among MIs in volatile elements like H_2O and Li (e.g. Figure 9) than is present in less mobile trace elements.
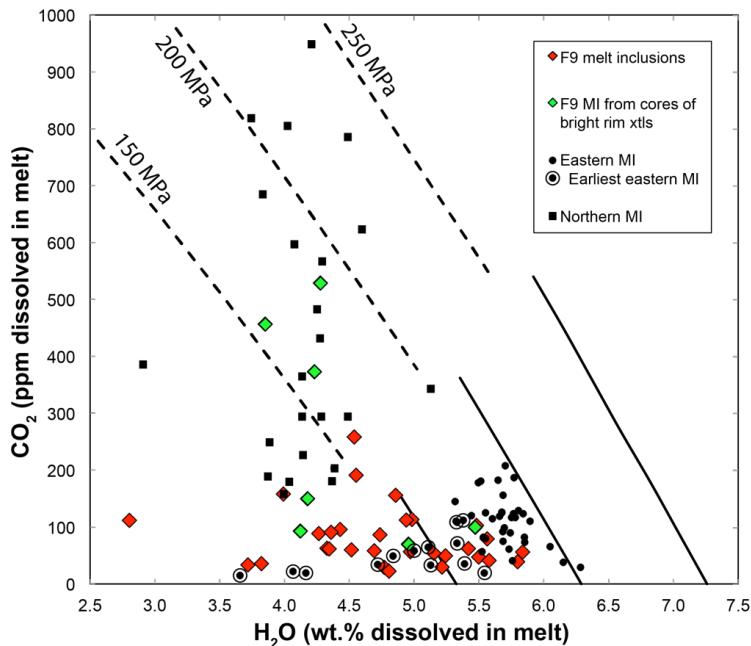

Figure 7. Bishop Tuff dissolved total H_2O and CO_2 contents from quartz-hosted MIs. Data plotted are fall unit F9 (red and green diamonds, this study), plus northern Ig2 (black squares), and eastern Ig2 materials (black filled circles) from Wallace et al. (2013) and Roberge et al. (2013). Earliest portions of the Bishop Tuff and likely from the shallowest depths are shown as target symbols (from Ig1Eb and fall units F1-F4). Diagonal lines are isobars for H_2O and CO_2 contents of H_2O-CO_2 gas saturated rhyolitic melt at 250, 200, and 150 MPa. Dashed lines are isobars calculated at 790 ˚C (deepest Bishop Tuff), and solid lines are isobars calculated at 725 ˚C (shallowest Bishop Tuff). Temperatures from Hildreth and Wilson (2007) and Chamberlain et al., 2014a.

CHAPTER IV

DISCUSSION

Compositional variations within F9

F9 melt inclusions contain variations in trace element (Figures 5, 6 and

supplemental files included with this thesis) and volatile (Figure 7) concentrations larger

than those of any other fall unit within the Bishop Tuff. Most F9 MI compositions fall

within the range of eastern ignimbrite (Ig2Ea, Ig2Eb packages of Wilson and Hildreth

1997) MI compositions, with a lesser proportion similar to the northern lobe values.

Some northern ignimbrite packages (e.g. Ig2Na and Ig2NWa: Wilson and Hildreth 1997)

have a large range in trace elements similar to that of the F9 MIs (Figures 5 and 9).

However, all the northern ignimbrite packages contain matrix glasses that are less

evolved (or overlapping in one exception) than their associated MIs (Roberge et al.

2013), whereas F9 matrix glasses are typically similar to or more evolved than their MI

compositions (upper two panels of Figure 6). These observations indicate that the melt

compositions sampled in the F9 represent a mixture of material from multiple levels

and/or laterally adjacent regions in the Bishop magma reservoir.

If F9 sampled at location 764 is, from the field relationships, interpreted as a

plinian fall deposit equivalent of later (Ig 2) eastern and northern ignimbrites, we might

expect to see more of a range in F9 matrix glass trace element compositions into the less

evolved end of the spectrum reported from the northern lobes (Roberge et al. 2013;

Chamberlain et al. 2015). However, we only found a few matrix glass compositions in F9

that plot at the less evolved end of the MI and matrix glass compositional array (Figure

6). One possibility to explain this apparent lack of less evolved matrix glass compositions

is that less evolved pumices are more prevalent in F9 but under-sampled in this study. Explanations could include a lack of adequate sample size or a sampling bias because the most glassy and vesicle-poor pumice fragments were preferentially picked for their increased likelihood of having solid glass regions large enough for LA-ICP-MS analysis. Another explanation is that the pumices in the northern lobe are quite dense, representing magma that was shattered and erupted laterally during eruption without much material getting entrained in a plinian plume (Wilson, pers. comm.). This would mean that relatively less material would have been fed into the high plume from the northern lobes, so deposition at location 764 would preferentially be from eastern vent sources. Despite the limited matrix glass compositional diversity, F9 melt inclusions record signatures of both northern and eastern ignimbrite lobes, demonstrating that eastern and northern Ig 2 lobes and F9 were erupted coevally with fractions of material from multiple levels in the magma reservoir incorporated into the plinian eruption column that was the source of F9.

Combining compositions and textures to reveal mixing and eruption behavior

The CL textures of the total population of quartz crystals from fall unit F9 differ from the those reported in Peppard et al. (2001), Roberge et al. (2013), and Chamberlain et al. (2014a). These workers reported that quartz crystals with bright rims occurred in high proportions in pumices from all the northern ignimbrite packages, whereas the bright rims were rare and thin, or entirely absent in eastern ignimbrite packages and fall units F1 to lower F9. Past workers may have failed to find bright rims in F9 quartz because F9 has been comparatively under sampled and because they sampled more proximal exposures of F9 and did not consider F9 at higher stratigraphic levels (i.e. locality 764). Instead, quartz crystals studied here from F9 have significant proportions

with both thick and thin bright-CL rims (Figure 2), though a majority have no bright-CL rims. This diversity within individual layers within the one fall unit suggests that its quartz crystals represent a mixed population from different parts of the Bishop magma system that must have been physically mixed during eruption in the plinian column before fall out and deposition.

In many locations around Long Valley caldera, F9 directly overlays Ig1E and its deposition is truncated by deposition of Ig2E on top, often in exposures less than 1 m thick (Wilson and Hildreth 1997). The stratigraphic levels reached by previous workers in unit F9 are thus limited by the influx of ignimbrite deposition. However, beyond the range of ignimbrite deposition, at location 764 in the case of this study (Figure 1), F9 accumulated to over 2 m thickness (and has a top truncated by erosion). Because of its extended stratigraphy in this distal location, and incorporation of MI compositions and quartz textures otherwise only seen in ignimbrite from the northern lobes (Ig2N and Ig2NW), we can conclude that the plinian plume that gave rise to the F9 fall deposits was present during the concurrent eruption of both eastern and northern Ig2 lobes. On the basis of accidental lithic lithologies found in the eruption products, eruption of Ig1 packages and fall units F1-F7 and almost all of F8 occurred from an initial vent location in the south-eastern sector of what became the caldera (Hildreth and Mahood 1986). Lithic clasts (crystal-poor obsidian and felsite) derived from pre-caldera Glass Mountain rhyolite eruptives then are additionally present in all Ig2 ignimbrite packages and the uppermost F8 and all of F9 fall deposits, The incoming of these Glass Mountain lithologies was thus taken to indicate migration of the vent and the development of multiple sources around the developing ring fracture (Hildreth and Mahood 1986). After

27

starting in the southeast portion of the ring fracture, vents opened up in the northwest part of the caldera, and then both vent regions extended towards Glass Mountain, incorporating lithics from its lavas and volcaniclastic debris fans (Wilson and Hildreth 1997; Hildreth and Wilson 2007). The presence of Glass Mountain lithics in both eastern and northern ignimbrites implies that different parts of the magma body were involved in the eruption at the same time and contributing to both ignimbrite flows and plinian fall deposits. The Bishop Tuff magma reservoir was likely both vertically and laterally variable and geometrically complex. Wallace et al. (1999) and Chamberlain et al. (2015) presented geometrically scaled models for the magma chamber that included a stepped roof such that the Ig2 eastern and northern ignimbrite packages would have come from the same connected system (cf. Gualda and Ghiorso 2013) but could erupt laterally independently of each other without occurring as interbedded deposits. This model, originally proposed by Wallace et al. (1999), makes the most sense in explaining how Ig2E and Ig2N packages could have erupted concurrently.

Many of the least evolved (lower Nb/Ce and Rb/Ce) melt inclusions from quartz crystals in fall unit F9 occur in the dark-CL quartz cores surrounded by bright-CL rims, but an additional subset occurs within crystals that completely lack bright rims. These observations together are important in demonstrating that the less evolved rhyolite compositions were present deeper in the magma reservoir prior to the later mixing events that produced the brightest CL rims. They also show that not all of the quartz with less evolved melt inclusions interacted with the 'bright-rim' magma(s). The less evolved compositions of MIs in rimmed and non-rimmed quartz crystals presented here are similar to the core MI compositions of many late northern ignimbrite samples from

28

Roberge et al. (2013). The latter were used to confirm that the host quartz cores did not come from the same population as quartz from Ig 1 deposits to the east. These observations, coupled with the continuously variable range in melt inclusion compositions reinforce the view that there was compositional zonation into the deeper part of the Bishop magma body, reflecting both a longer-term compositional gradient (seen also, for example in the two-feldspar compositions and temperatures; Chamberlain et al. 2015) and also a prolonged interaction with less-evolved input magma(s) that gave rise to the CL-bright rims.

Dark gray and swirly (mixed dark and light) pumices are present in minor proportions in all ignimbrite packages and provide a visible snapshot of late, less evolved inputs into the system. Their matrix glass Rb/Ce and Nb/Ce values (Figure 6) show a compositional range spanning all normal Bishop pumice, reflecting the late-stage influxes of less-evolved magma(s) and varying degrees of mixing in widespread regions of the Bishop Tuff system (Hildreth and Wilson 2007; Roberge et al. 2013; Chamberlain et al. 2015). Juvenile dacite lithics, found only in Ig2NWb, have the least evolved chemistry (Rb/Ce, Nb/Ce in Figure 6 as well as high Ba, Sr, and Ti) of all Bishop Tuff glasses and therefore best approximate of the type of late magma inputs that created the bright-CL rims on quartz crystals (Hildreth and Wilson 2007; Chamberlain et al. 2015).

Chamberlain et al. (2014a) conducted a detailed study on the exterior zoning of multiple Bishop Tuff crystal phases. They concluded that the 'bright-rim' magma(s) were introduced to the system in multiple influxes over the course of ~500 years prior to eruption. Using samples from Ig2N and Ig2NW ignimbrite packages, Ti-in-quartz models yielded estimated timescales of 1-100 years for quartz rim formation, while timescales

derived from Ba/Sr profiles in sanidine and Fe-Mg profiles in orthopyroxene fell within

an order of magnitude of this range (Chamberlain et al. 2014a). Ti-in-quartz diffusion

models from bright-rim F9 quartz phenocrysts measured in this study agree well with

these findings (Figure 8). Unit F9 timescales were modeled for quartz with both thick and

thin outer bright rims, and all gave timescales of within 100 years of eruption. F9 bright

rims yielded estimate that vary from 15-83 years with one crystal recording an earlier

growth event ~310 years before eruption. The agreement between the results from this

study and those of Chamberlain et al. (2014a,b) provides further confirmation that

portions of fall unit F9 contain quartz crystals that have a shared history with the northern

Ig2 ignimbrites. The different rim thicknesses could indicate crystals coming from

different locations in the magma system that experienced different degrees of interaction

with 'bright-rim' magmas within roughly the same time period. Zircons in the system

have less evolved rims that record ages of up to ~10 kyr (Chamberlain et al. 2014b),

which may be recording much earlier primitive influxes that could have formed the

parent magmas of the least evolved dark-CL quartz cores in F9 and Ig2 and indicate that

the bright-rim magma interacted with the main Bishop body over a gradual time period.
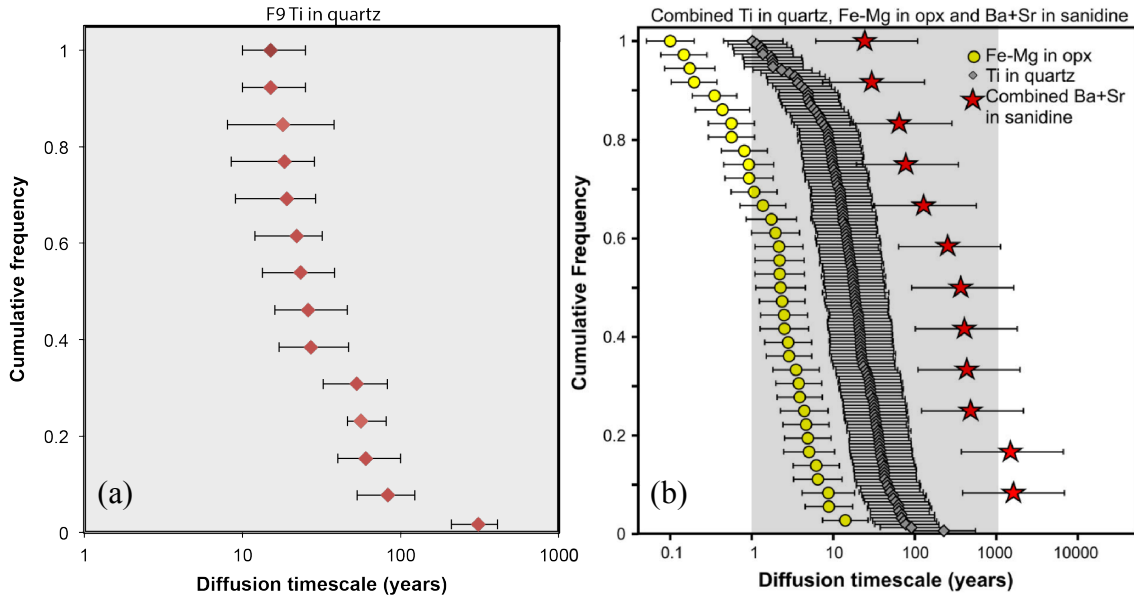
Figure 8. **a)** Cumulative frequency graph with the timescales derived from unit F9 bright-rim quartz crystals, with the associated uncertainties. **b)** cumulative frequency graph of timescales from three mineral phases and uncertainties from Chamberlain et al. (2014a). Gray field in (b) corresponds to the x-axis extent in a).

Volatile contents in F9 MIs and their implications

Published data from Bishop Tuff quartz-hosted MIs show that pre-eruptive gradients in both dissolved H_2O and CO_2 existed throughout the magma reservoir. Eastern Ig 1 and Ig 2 have concentrations of ~5-6 wt.% H_2O and 10-200 ppm CO_2, whereas northern units have ranges of ~3.5-5 wt.% H_2O and 38-1085 ppm CO_2 (Wallace et al. 1999; Roberge et al. 2013). Melt inclusions contained within bright rim overgrowths have the highest CO_2 concentrations as well as elevated Ba, Sr, and Ti (Figure 10 of Roberge et al. 2013). The Bishop magma reservoir was inferred to be gas-saturated at the time of crystallization on the basis of an inverse correlation between CO_2 and incompatible trace element abundances. From this, and assuming gas saturation, the volatile abundance data lead to pressure estimates of ~150-280 MPa for the Bishop system as sampled (Wallace et al. 1999). The majority of F9 MIs measured for this study

31

have lower CO_2 over a wide range of H_2O values, overlapping much of the eastern ignimbrite data range (Figure 7). A subset of F9 MIs falls in the much higher CO_2 region with values comparable to the MIs from northern Ig2 samples that were trapped at higher pressures and temperatures. These highest CO_2 values measured in both F9 and the northern ignimbrite Ig2 packages dominantly come from bright-rimmed quartz crystals. However, the northern ignimbrite bright-rim MIs come from within the rims themselves whereas the F9 MIs come from the cores of bright-rim crystals. The less evolved F9 cores grew in a part of the reservoir that was less evolved before the influence of any bright-rim magma influxes.

The lowest CO_2 and H_2O values from F9 MIs overlap with those from the earlier Ig1E unit and fall units F1-F4 ("Earliest eastern MI" on Figure 7) and come from both bright-rimmed and non-rimmed crystals. The MIs with low volatile abundances from the earliest portions of the Bishop Tuff and the non-rimmed F9 quartz are inferred to have come from shallow regions of the magma reservoir where they would have experienced pressure-driven volatile loss (Wallace et al. 1999; Liu et al. 2007; Myers et al. 2019). Northern Ig 2 and F9 melt inclusions with low volatile contents from quartz crystals with bright rims could have experienced water loss when their host crystals interacted with 'bright-rim' magmas via post-entrapment diffusive re-equilibration. At magmatic temperatures, melt inclusions can lose H_2O rapidly on timescales of days to weeks if they are significantly out of equilibrium with their host melt (Severs et al. 2007). This is likely in the deep portions of the Bishop magma because the less evolved inputs had high CO_2 contents and relatively low H_2O (Wallace et al. 1999; Roberge et al. 2013).
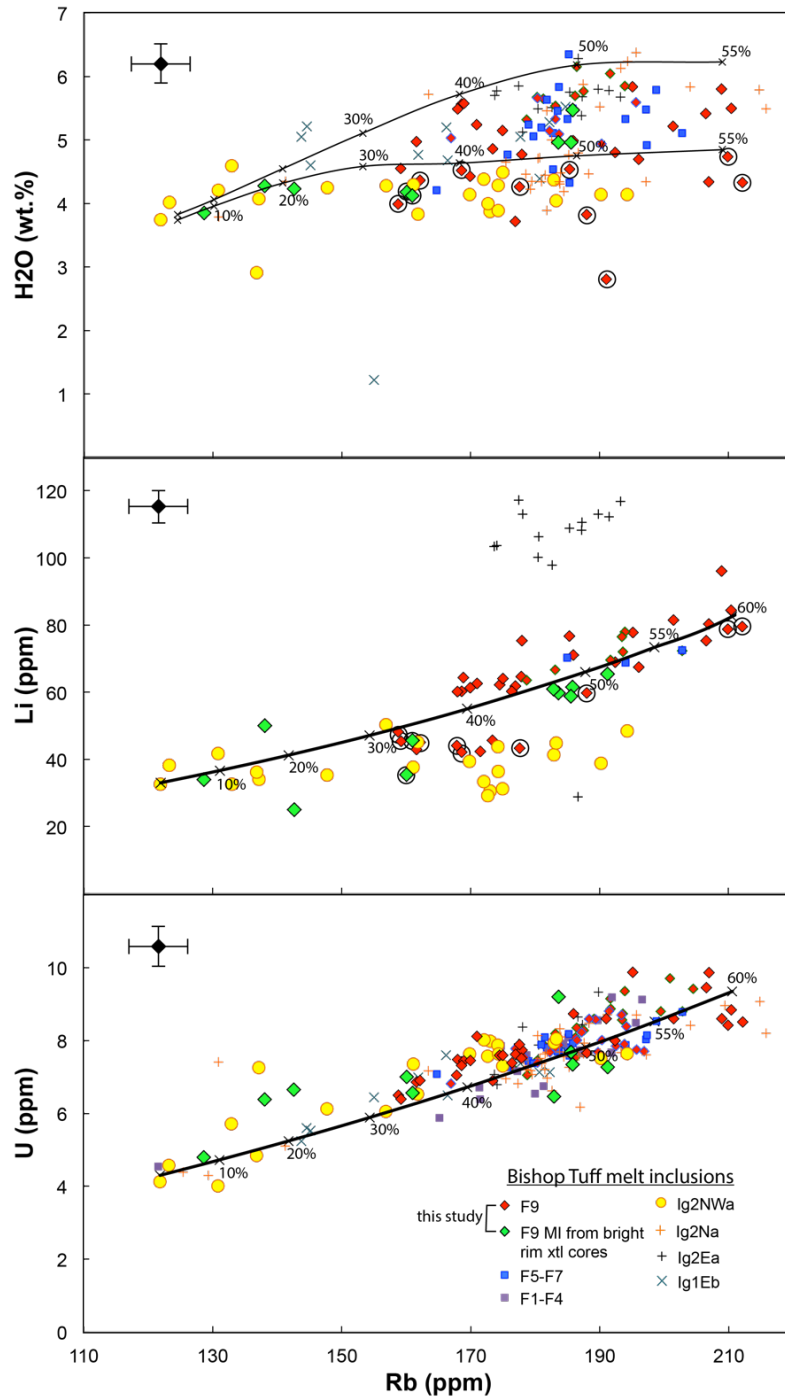
Figure 9. H$_2$O, Li, and U concentrations versus Rb. Includes data from Wallace et al. (1999) and Roberge et al. (2013). Symbols explained in lower panel. Black curves are equilibrium crystallization calculations with starting compositions approximating the least evolved Bishop melt inclusions using the following bulk partition coefficients (D): D = 0.298 for Rb, D = 0.1 for U, D = 0 for Li (all from Roberge et al. 2013), and varying H$_2$O D values for each crystallization step. The upper H$_2$O v. Rb curve models an initial water content of 3%, making the system just barely vapor saturated; the lower curve uses 4% initial water for a reasonable vapor oversaturated modes of the Bishop Tuff system. H$_2$O values are predicted to fall within the upper and lower curves. Black circles surround F9 data points that fall below the model curves in both the H$_2$O v. Rb and Li v. Rb plots.

Quartz-hosted MIs from portions of the northern ignimbrite lobes and F9 have low H_2O values (Figure 9) despite having high Rb concentrations (Wallace et al. 1999; Roberge et al. 2013). Both H_2O and Rb are moderately incompatible in the Bishop system (Hildreth 1979), so they should positively co-vary. To test for diffusive losses, we plot H_2O and Li against Rb (Figure 9), following Myers et al. (2019). Li, like H_2O, is also incompatible in the Bishop Tuff magma and diffuses rapidly in quartz at magmatic temperatures (Verhoogen 1952; Charlier et al. 2012). Both H_2O and Li values are scattered when plotted versus Rb, differing as such from the tight positive or negative correlations of other major and trace elements in the system that diffuse much slower in quartz (e.g. U vs. Rb: Figure 9). The plots with H_2O and Li versus Rb seem to show a positive correlation until a portion of the MI data fall off the crystallization trends at higher Rb values. The majority of the MI compositions falling off the trends come from Ig2NWa (late northern ignimbrite with bright rims on nearly all quartz phenocrysts, as reported in Wallace et al. 1999, Peppard et al. 2001, and Chamberlain et al. 2015) and fall unit F9 (presented here), of which many come from the darker cores of crystals with bright CL rims. It is likely that H_2O and Li followed the equilibrium crystallization trends with Rb but were partially lost due to diffusive re-equilibration after entrapment in some quartz that interacted with less evolved magmas somewhere deep in the system.

CHAPTER V

CONCLUSIONS

Quartz-hosted melt inclusions sampled from within Bishop fall unit F9 at localities 764 and 876 (Figure 1) show a range of compositions that include the distinct chemical signatures of material erupted from both the northern (crystal-richer, less evolved) and eastern (crystal-poorer, more evolved) Ig 2 ignimbrite packages. Trace element data for accompanying unit F9 matrix glasses show a similar to or slightly more evolved compositions as the melt inclusions (e.g. as expressed in Rb/Ce, Nb/Ce, and U values) with the exception of a few matrix glasses near the less evolved end of the MI array. Finding melt inclusions in the F9 fall deposits that have compositional similarity to those in both northern and eastern ignimbrite package samples implies that all the Ig2 packages were coevally erupted, as suggested by previous field data and stratigraphic correlations (Wilson and Hildreth 1997; Hildreth and Wilson 2007). Melt inclusion compositions and crystal zoning within quartz crystals from fall unit F9 and the Ig2 packages also suggest a complex history of magma mixing and mingling in many parts of the system over multiple time periods leading up to the eruption.

Overall the range in MI compositions and textures in the host quartz crystals within fall unit F9, when compared to existing Bishop Tuff data, have three primary implications.

(1) Unit F9 is the fall equivalent to the northern and eastern ignimbrite Ig2 packages, incorporating material from a range of levels in the magma chamber and fed from multiple vent sources around the ring fracture of the developing caldera.

35

(2) Quartz rims and MI compositions in quartz cores record evidence of numerous inputs of less evolved melts ('bright rim magma') into the magma reservoir, The inputs represented in the quartz crystals mostly occurred <100 years before eruption and are represented by the bright-CL rims on quartz and likely the swirly pumices. However, the corresponding evidence from other mineral phases (e.g. sanidine and zircon) yield longer timescales and it is inferred that the quartz crystals represent a skewed record due to the ease with which they can be dissolved and regrown.

(3) Melt inclusions in quartz crystals that were exposed to the 'bright-rim' magma or stored at very shallow depths are inferred to have experienced some loss of H_2O and Li due to post-entrapment diffusive re-equilibration.

REFERENCES CITED

Anderson, Jr. AT (1991) Hourglass inclusions : Theory and application to the Bishop Rhyolitic Tuff. Am Mineral 76:530–547

Anderson, Jr. AT, Davis AM, Lu F (2000) Evolution of Bishop Tuff Rhyolitic Magma Based on Melt and Magnetite Inclusions and Zoned Phenocrysts. J Petrol 41:449–473. doi: 10.1093/petrology/41.3.449

Bachmann O, Huber C (2016) Silicic magma reservoirs in the Earth's crust. Am Mineral 101:2377–2404. doi: 10.2138/am-2016-5675

Bindeman IN, Valley JW (2002) Oxygen isotope study of the Long Valley magma system, California: isotope thermometry and convection in large silicic magma bodies. Contrib to Mineral Petrol 144:185–205. doi: 10.1007/s00410-002-0371-8

Blundy J, Cashman K (2001) Ascent-driven crystallisation of dacite magmas at Mount St Helens, 1980-1986. Contrib to Mineral Petrol 140:631–650. doi: 10.1007/s004100000219

Chamberlain KJ, Morgan DJ, Wilson CJN (2014a) Timescales of mixing and mobilisation in the Bishop Tuff magma body: Perspectives from diffusion chronometry. Contrib to Mineral Petrol 168:1–24. doi: 10.1007/s00410-014-1034-2

Chamberlain KJ, Wilson CJN, Wallace PJ, Millet MA (2015) Micro-analytical perspectives on the bishop tuff and its magma chamber. J Petrol 56:605–640. doi: 10.1093/petrology/egv012

Chamberlain KJ, Wilson CJN, Wooden JL, et al (2014b) New Perspectives on the BishopTuff from Zircon Textures, Ages and Trace Elements. J Petrol 55:395–426. doi: 10.1093/petrology/egt072

Charlier BLA, Morgan DJ, Wilson CJN, et al (2012) Lithium concentration gradients in feldspar and quartz record the final minutes of magma ascent in an explosive supereruption. Earth Planet Sci Lett 319–320:218–227. doi: 10.1016/j.epsl.2011.12.016

Cherniak DJ, Watson EB, Wark DA (2007) Ti diffusion in quartz. Chem Geol 236:65–74. doi: 10.1016/j.chemgeo.2006.09.001

Costa F, Morgan D (2010) Time constraints from chemical equilibration in magmatic crystals. In: Dosseto A, Turner SP, Van Orman JA (eds) Timescales of Magmatic Processes: From Core to Atmosphere. Wiley, pp 125–159

Dixon JE, Holloway JR (1995) An experimental study of water and carbon dioxide solubilities in mid-ocean ridge basaltic liquids. Part II: Applications to degassing. J Petrol 36:1607–1631. doi: 10.1093/oxfordjournals.petrology.a037268

Donovan JJ, Kremser D, Fournelle JH, Goemann K (2007) Probe for Windows user's guide and reference, enterprise edition. Probe Software Inc., Eugene, OR

Dunbar NW, Hervig RL (1992) Petrogenesis and volatile stratigraphy of the Bishop Tuff: Evidence from melt inclusion analysis. J Geophys Res 97:129–150. doi: 10.1029/92jb00764

Evans BW, Hildreth W, Bachmann O, Scaillet B (2016) In defense of magnetite-ilmenite thermometry in the Bishop Tuff and its implication for gradients in silicic magma reservoirs. Am Mineral 101:469–482. doi: 10.2138/am-2016-5367

Ghiorso MS, Evans BW (2008) Thermodynamics of rhombohedral oxide solid solutions and a revision of the Fe-Ti two-oxide geothermometer and oxygen-barometer. Am J Sci 308:957–1039. doi: 10.2475/09.2008.01

Gualda GAR, Ghiorso MS (2013a) Low-Pressure Origin of High-Silica Rhyolites and Granites. J Geol 121:537–545. doi: 10.1086/671395

Gualda GAR, Ghiorso MS (2013b) The Bishop Tuff giant magma body: An alternative to the Standard Model. Contrib to Mineral Petrol 166:755–775. doi: 10.1007/s00410-013-0901-6

Gualda GAR, Ghiorso MS, Lemons R V, Carley TL (2012a) Rhyolite-MELTS : a Modified Calibration of MELTS Optimized for Silica-rich, Fluid-bearing Magmatic Systems. J Petrol 53:875–890. doi: 10.1093/petrology/egr080

Gualda GAR, Pamukcu AS, Ghiorso MS, et al (2012b) Timescales of Quartz crystallization and the longevity of the Bishop Giant Magma body. PLoS One 7:e37492. doi: 10.1371/journal.pone.0037492

Hildreth W (1979) The Bishop Tuff : Evidence for the origin of compositional zonation in silicic magma chambers. Geol Soc Am Spec Pap 180:43–76. doi: 10.1130/SPE180-p43

Hildreth W (2004) Volcanological perspectives on Long Valley, Mammoth Mountain, and Mono Craters: Several contiguous but discrete systems. J Volcanol Geotherm Res 136:169–198. doi: 10.1016/j.jvolgeores.2004.05.019

Hildreth W, Mahood GA (1986) Ring-fracture eruption of the Bishop Tuff. Geol Soc Am Bull 97:396–403

Hildreth W, Wilson CJN (2007) Compositional zoning of the bishop tuff. J Petrol 48:951–999. doi: 10.1093/petrology/egm007

Jochum KP, Stoll B, Herwig K, et al (2006) MPI-DING reference glasses for in situ microanalysis: New reference values for element concentrations and isotope ratios. Geochemistry, Geophys Geosystems 7:. doi: 10.1029/2005GC001060

Jochum KP, Willbold M, Raczek I, et al (2005) Chemical Characterisation of the USGS Reference Glasses and BIR-1G Using EPMA , ID-TIMS , ID-ICP-MS and LA-ICP-MS. Geostand Geoanalytical Res 29:285–302. doi: 10.1111/j.1751-908X.2005.tb00901.x

Liu Y, Anderson AT, Wilson CJN (2007) Melt pockets in phenocrysts and decompression rates of silicic magmas before fragmentation. J Geophys Res Solid Earth 112:1–12. doi: 10.1029/2006JB004500

Lu F, Anderson AT, Davis AM (1992) Melt inclusions and crystal-liquid separation in rhyolitic magma of the Bishop Tuff. J Petrol 110:113–120

Matthews NE, Huber C, Pyle DM, Smith VC (2012a) Timescales of magma recharge and reactivation of large silicic systems from ti diffusion in quartz. J Petrol 53:1385–1416. doi: 10.1093/petrology/egs020

Matthews NE, Pyle DM, Smith VC, et al (2012b) Quartz zoning and the pre-eruptive evolution of the ~ 340-ka Whakamaru magma systems , New Zealand. Contrib to Mineral Petrol 163:87–107. doi: 10.1007/s00410-011-0660-1

Michael PJ (1983) Chemical differentiation of the Bishop Tuff and other high-silica magmas through crystallization processes. Geology 11:31–34. doi: 10.1130/0091-7613(1983)11<622:CAROCD>2.0.CO;2

Nichols ARL, Wysoczanski RJ (2007) Using micro-FTIR spectroscopy to measure volatile contents in small and unexposed inclusions hosted in olivine crystals. Chem Geol 242:371–384. doi: 10.1016/j.chemgeo.2007.04.007

Peppard BT, Steele IM, Davis AM, et al (2001) Zoned quartz phenocrysts from the rhyolitic Bishop Tuff. Am Mineral 86:1034–1052

Petrone CM, Bugatti G, Braschi E, Tommasini S (2016) Pre-eruptive magmatic processes re-timed using a non-isothermal approach to magma chamber dynamics. Nat Commun 7:1–11. doi: 10.1038/ncomms12946

Roberge J, Wallace PJ, Kent AJR (2013) Magmatic processes in the Bishop Tuff rhyolitic magma based on trace elements in melt inclusions and pumice matrix glass. Contrib to Mineral Petrol 165:237–257. doi: 10.1007/s00410-012-0807-8

Severs MJ, Azbej T, Thomas JB, et al (2007) Experimental determination of H 2 O loss from melt inclusions during laboratory heating: Evidence from Raman spectroscopy. Chem Geol 237:358–371. doi: 10.1016/j.chemgeo.2006.07.008

Stockli DF, Dumitru TA, McWilliams MO, Farley KA (2003) Cenozoic tectonic evolution of the White Mountains, California and Nevada. Bull Geol Soc Am 115:788–816. doi: 10.1130/0016-7606(2003)115<0788:CTEOTW>2.0.CO;2

Wallace PJ, Anderson, Jr. AT, Davis AM (1999) Gradients in H2O, CO2, and exsolved gas in a large-volume silicic magma system: Interpreting the record preserved in melt inclusions from the Bishop Tuff. J Geophys Res 104:20097–20122. doi: 10.1029/1999JB900207

Wallace PJ, Dufek J, Anderson AT, Zhang Y (2003) Cooling rates of Plinian-fall and pyroclastic-flow deposits in the Bishop Tuff: inferences from water speciation in quartz-hosted glass inclusions. Bull Volcanol 65:105–123. doi: 10.1007/s00445-002-0247-9

Wark DA, Hildreth W, Spear FS, et al (2007) Pre-eruption recharge of the Bishop magma system. Geology 35:235–238. doi: 10.1130/G23316A.1

Wark DA, Watson EB (2006) TitaniQ: A titanium-in-quartz geothermometer. Contrib to Mineral Petrol 152:743–754. doi: 10.1007/s00410-006-0132-1

Wilson CJN, Hildreth W (1997) The Bishop Tuff: New Insights From Eruptive Stratigraphy. J Geol 105:407–440. doi: 10.1086/515937

Wysoczanski R, Tani K (2006) Spectroscopic FTIR imaging of water species in silicic volcanic glasses and melt inclusions: An example from the Izu-Bonin arc. J Volcanol Geotherm Res 156:302–314. doi: 10.1016/j.jvolgeores.2006.03.024

Zhang Y, Belcher R, Ihinger PD, et al (1997) New calibration of infrared measurement of dissolved water in rhyolitic glasses. Geochim Cosmochim Acta 61:3089–3100. doi: 10.1016/S0016-7037(97)00151-8